



SO₂-tolerant mesoporous iron oxide supported bimetallic single atom catalyst for methanol removal

Wenbo Pei, Kuan Yang, Jiguang Deng ^{*}, Yuxi Liu, Zhiqian Hou, Jia Wang, Yuan Feng, Xiaohui Yu, Hongxing Dai

Beijing Key Laboratory for Green Catalysis and Separation, Key Laboratory of Beijing on Regional Air Pollution Control, Key Laboratory of Advanced Functional Materials, Education Ministry of China, Faculty of Environment and Life Science, Beijing University of Technology, Beijing 100124, China



ARTICLE INFO

Keywords:
Bimetallic single-atom catalyst
Mesoporous iron oxide
Volatile organic compound oxidation
SO₂ resistance
Reaction mechanism

ABSTRACT

Among the single-atom catalysts (SACs), the bimetallic single-atom catalysts play an increasingly promising role in the oxidative removal of volatile organic compounds (VOCs) due to their high efficiency. However, it remains a significant challenge to resist SO₂ poisoning in industrial applications. In this work, we report (i) the synthesis of three-dimensionally ordered mesoporous Fe₂O₃-supported bimetallic AuPt single-atom (denote as Au₁Pt₁/meso-Fe₂O₃) catalyst via a modified polyvinyl alcohol-protected reduction route; (ii) catalytic performance of the catalysts for methanol oxidation; and (iii) catalytic and SO₂-resistant mechanism. It was found that compared with Pt₁/meso-Fe₂O₃ and Pt_{np}/meso-Fe₂O₃, Au₁Pt₁/meso-Fe₂O₃ exhibited better catalytic activity for methanol combustion, with the temperature at 90% methanol conversion, TOF_{noble metal} at 120 °C, and apparent activation energy being 137 °C at a space velocity of 20 000 mL g⁻¹ h⁻¹, 6.51 × 10⁻² s⁻¹, and 36 kJ mol⁻¹, respectively. The enhanced activity was associated with the improved reducibility, methanol adsorption ability, and strong interaction between noble metal and support. The reaction pathway was deduced to follow a sequence of methanol → methoxy species → formaldehyde → formic acid → CO₂ and H₂O. Furthermore, the order of SO₂ resistance was Au₁Pt₁/meso-Fe₂O₃ > Pt₁/meso-Fe₂O₃ > Pt_{np}/meso-Fe₂O₃. The good SO₂ resistance of the Au₁Pt₁/meso-Fe₂O₃ catalyst was attributed to the Au–Pt bimetallic single atoms uniformly dispersed on the meso-Fe₂O₃ with the strong ability of sulfate decomposition and the protection of the active sites by meso-Fe₂O₃ as a sacrificial site. This work presents a novel way for developing high-performance catalysts for VOCs elimination in the presence of SO₂.

1. Introduction

The emission of volatile organic compounds (VOCs) in large quantities lead to air pollution and harm human health [1–6]. Methanol is a common solvent in industry, a raw material in the synthesis of chemical products, and an additive in automobile fuels. The petrochemical and rubber processing industries could emit emissions containing methanol and SO₂ [7–9]. Among all of the abatement pathways to the elimination of low-concentration VOCs, catalytic oxidation possesses the advantages of low energy consumption, good flexibility, and high efficiency [10, 11]. Bimetallic catalysts generally exhibit good activity, high selectivity, and strong anti-poisoning ability in the removal of VOCs [12, 13]. Due to the synergistic effect of two metals, bimetallic single-atom catalysts possess different geometric and electronic structures that render them to exhibit excellent catalytic performance in various reactions [14–16].

The bimetallic single-atom catalysts are usually generated by a highly active or expensive metal (with a small amount) with a relatively less active or inexpensive metal in the form of a single atom [17–22]. For instance, Zhao et al. [23] designed a bifunctional Fe/Cu bimetallic single-atom catalyst anchored on N-doped porous carbon (FeCu-SA-NPC), and concluded that it can effectively degrade and mineralize chlorinated organic pollutants by benefiting from the synergistic interaction between dechlorination of single-atom Cu and ·OH oxidation on single-atom Fe. The supported noble metal (e. g. Pt or Au) catalysts usually activate lattice oxygen at the interface between noble metal and support, thus promoting the transformation of surface oxygen species and reducing the conversion temperature of VOCs oxidation [24]. In addition, there are few reports on the construction of Pt and Au bimetallic catalysts, especially for the removal of VOCs.

As a common component of industrial exhaust, SO₂ usually poison

* Corresponding authors.

E-mail addresses: jgdeng@bjut.edu.cn (J. Deng), hxdai@bjut.edu.cn (H. Dai).

the catalysts, particularly supported noble metal catalysts by forming sulfites and/or sulfates of noble metals on the catalyst surface. Up to now, the strategies to improve sulfur resistance of the catalysts mainly include increasing acidity to reduce adsorption of sulfur oxides and constructing the sacrifice sites to protect the active sites from poisoning [25–27]. For example, the selective catalytic reduction (SCR) performance of the FeTiO_x catalysts was enhanced in the SO_2 atmosphere due to the enhancement in acid strength because of the interaction of sulfate species with the iron sites [28]. The addition of Fe in $\text{Fe}_\delta\text{Ce}_{1-\delta}\text{VO}_4$ could effectively suppress SO_2 adsorption, endowing it with good SO_2 tolerance in the SCR of NO_x [29]. Moreover, the Fe_2O_3 -modified halloysite-supported CeO_2-WO_3 catalyst indicates high sulfur-poisoning resistance in NO_x reduction, since SO_2 first reacted with outer layer of Fe_2O_3 to prevent the deposition of sulfates at the active CeO_2 and WO_3 components [30]. In our group's previous work, we successfully prepared a bimetallic single-atom palladium–cobalt ($\text{Pd}_1\text{Co}_1/\text{Al}_2\text{O}_3$) catalyst and found it showed better sulfur dioxide tolerance than $\text{Pd}/\text{Al}_2\text{O}_3$ in the combustion of benzene, which was attributed to the unique $\text{Pd}-\text{Co}$ single-atom active sites that exhibited good regeneration performance [31]. We also prepared the ZrO_2 -supported platinum–palladium bimetallic nanoparticles catalysts and the mesoporous Na_xMnO_y -supported platinum–cobalt bimetallic single-atom catalysts with good SO_2 resistance in methane propane and propane combustion, respectively [32,33]. However, in situ characterization on the effect of SO_2 on catalyst is not comprehensive, and the study of effect of SO_2 on support is not thorough.

Although we previously have paid much attention for the catalytic removal of CO , VOCs , and CH_4 using the supported noble metal catalysts, the sulfur dioxide tolerance of the adopted catalysts is a huge challenge. Herein, we report the controllable preparation, characterization, and catalytic performance for methanol removal of bimetallic $\text{Au}-\text{Pt}$ single-atom dispersed on the three-dimensionally ordered mesoporous Fe_2O_3 catalyst (denote as $\text{Au}_1\text{Pt}_1/\text{meso-Fe}_2\text{O}_3$). $\text{Au}_1\text{Pt}_1/\text{meso-Fe}_2\text{O}_3$ exhibits high catalytic activity for the methanol oxidation, and excellent tolerance in the presence of SO_2 , superior to the meso- Fe_2O_3 supported Pt nanoparticles and Pt single-atom catalysts (denote as $\text{Pt}_{\text{np}}/\text{meso-Fe}_2\text{O}_3$ and $\text{Pt}_1/\text{meso-Fe}_2\text{O}_3$). Further, various characterization experiments, such as X-ray photoelectron spectroscopy (XPS), fourier-transform infrared spectroscopy (FTIR), temperature-programmed techniques (He-TPD, and Methanol-TPD), temperature-programmed surface reaction (TPSR), in situ diffuse reflectance infrared Fourier transform spectroscopy (in situ DRIFTS), and in situ GC-MS online analytical technique were executed to probe the mechanism of the effect of SO_2 on noble metal active sites and meso- Fe_2O_3 support of catalysts. This work provides a way to improve the activity and SO_2 resistance of traditional supported noble metal Pt catalysts, and which is beneficial to the development of high-performance catalysts for VOCs elimination in the presence of SO_2 .

2. Experimental

2.1. Catalyst preparation

meso- Fe_2O_3 was synthesized using the KIT-6-templating method, as described previously [34]. The meso- Fe_2O_3 -supported Au_1Pt_1 bimetallic single-atom catalysts were synthesized via a modified polyvinyl alcohol (PVA)-protected reduction route. Typically, a desired amount of PVA was added to a mixed solution of $\text{Pt}(\text{NH}_3)_4(\text{NO}_3)_2$ and HAuCl_4 mixed solution (Pt/Au molar ratio = 3: 1, 1: 1 and 1: 3, respectively) with the PVA/noble metal mass ratio being 1.2: 1. Then 1.0 g of meso- Fe_2O_3 impregnated in methanol was added to the above solution, with the theoretical $\text{Au}-\text{Pt}$ loading being 0.12 wt%. After being vigorously stirred in an ice–bath for 4 h, a NaBH_4 aqueous solution was added to the above solution (noble metal/ NaBH_4 molar ratio = 1: 5). After stirring for 2 h, the solid powders were filtered, washed by ethanol, and dried at 80 °C for 12 h, hence obtaining the $\text{Au}_1\text{Pt}_1/\text{meso-Fe}_2\text{O}_3$ catalysts. The

supported Pt single-atom (denoted as $\text{Pt}_1/\text{meso-Fe}_2\text{O}_3$) catalyst was also prepared using the same method. Different from the preparation of the former catalyst, the precursor solution in the preparation process does not contain HAuCl_4 .

For comparison purpose, the meso- Fe_2O_3 -supported Pt NPs (denoted as $\text{Pt}_{\text{np}}/\text{meso-Fe}_2\text{O}_3$) catalyst was synthesized as follows: Quickly added NaBH_4 solution (0.1 g L^{-1}) to the mixed solution of PVA and H_2PtCl_6 aqueous solution under ice bath conditions (Pt/ NaBH_4 molar ratio = 1: 5), generating a dark-brown sol. Then added the desired amount of meso- Fe_2O_3 powders to the above solution (theoretical Pt = 0.12 wt%) and stirred for 5 h. The above mixture was filtered, washed, and dried at 80 °C overnight, thus obtaining the $\text{Pt}_{\text{np}}/\text{meso-Fe}_2\text{O}_3$ catalyst.

2.2. Catalyst characterization

X-ray diffraction (XRD), N_2 adsorption–desorption (BET), inductively coupled plasma–atomic emission spectroscopic (ICP–AES), high-resolution transmission electron microscopy (HR-TEM), Aberration corrected high angle annular dark field–scanning transmission electron microscopic (AC-HAADF–STEM), element mapping, X-ray photoelectron spectroscopy (XPS), hydrogen temperature-programmed reduction (H_2 -TPR), oxygen, methanol, SO_2 , and helium temperature-programmed desorption (O_2 -, Methanol-, SO_2 , and He-TPD), temperature-programmed oxidation (TPO), GC/MS online analyzer, Fourier transform infrared spectroscopy (FT-IR), in situ diffuse reflectance Fourier transform infrared spectroscopy (in situ DRIFTS), in situ CO adsorption, and metal dispersion measurements. The detailed characterization procedures are stated in the [Supplementary material](#).

2.3. Catalytic evaluation

Activity of the catalysts for methanol oxidation was evaluated using a continuous flow fixed-bed quartz tubular microreactor (*i.d.* = 6 mm). 250 mg of quartz sand (40–60 mesh) evenly mixed with 50 mg of the catalyst (40–60 mesh) was placed into the microreactor. The feeding gas composition was (1000 ppm methanol + 20 vol% O_2 + N_2 (balance)), with the space velocity (SV) being ca. 20 000 $\text{mL g}^{-1} \text{h}^{-1}$. Before the test, the catalyst was pretreated in an O_2 flow of 30 mL min^{-1} at 250 °C for 1 h. For the study of SO_2 effects, 40 or 100 ppm SO_2 from a steel cylinder containing SO_2 and nitrogen (balance) was fed into the reactor. The details can be seen from the [Supplementary material](#).

The conversion of methanol (X_{MeOH}) was defined as Eq. 1:

$$X_{\text{MeOH}} (\%) = \frac{C_{\text{in}} - C_{\text{out}}}{C_{\text{in}}} \times 100\% \quad (1)$$

where the C_{in} and C_{out} represent the inlet and outlet methanol concentrations in the feed stream, respectively.

The specific reaction rate (r_{MeOH} ($\mu\text{mol}/(\text{gnoble metal s})$)) was defined as Eq. 2:

$$r_{\text{MeOH}} = \frac{X_{\text{MeOH}} V_{\text{MeOH}}}{M_{\text{cat}} (\text{wt \%})} \quad (2)$$

where M_{cat} is the catalyst mass (g), and V_{MeOH} is the methanol flow rate (mol/s).

There were no considerable mass transfer limitations existence when methanol conversion $\leq 20\%$. In this work, methanol oxidation followed the first-order mechanism toward methanol concentration, and the empirical kinetic expression of the reaction rate equation can be defined as Eq. 3:

$$r = -kc = -A \exp(-\frac{E_a}{RT})c \quad (3)$$

where r , k , A , and E_a represent the reaction rate (mol/s), rate constant (s^{-1}), pre-exponential factor, and apparent activation energy (kJ/mol), respectively.

The turnover frequency (TOF_{noble metal} (s⁻¹)) based on the noble metal active sites can be calculated according to Eq. 4:

$$\text{TOF}_{\text{noble metal}} = \frac{X_{\text{MeOH}} V_{\text{MeOH}}}{N_{\text{noble metal}} D_{\text{noble metal}}} \quad (4)$$

where X_{MeOH} , V_{MeOH} , $N_{\text{noble metal}}$, and $D_{\text{noble metal}}$ represent the toluene conversion (%), methanol gas flow rate (mol/s), Au and/or Pt content (mol) in the sample, and dispersion (%) of the noble metal on the surface of the support, respectively.

3. Results and discussion

3.1. Catalytic performance and SO₂ resistance for methanol removal

As the simplest saturated monohydric alcohol, methanol is one of the basic organic raw materials and is widely used. A large amount of waste gas containing methanol vapor will be unavoidably discharged. As shown in Fig.S1, after testing the methanol oxidation activity of catalysts with different molar ratios of Au and Pt, we selected the sample with the best activity (Au/Pt molar ratio = 1:3) as the main research object.

Fig. 1a and S2 show catalytic activities and Arrhenius plots of the catalysts for methanol oxidation, respectively, and Table 1 summarizes methanol conversion temperatures, apparent activation energies (E_a), specific reaction rates, and turnover frequencies (TOFs) of the catalysts. Over the Au₁Pt₁/meso-Fe₂O₃ catalyst, the $T_{50\%}$ and $T_{90\%}$ were 96 and 137 °C, respectively. With the similar noble metal loadings, the bimetallic AuPt single-atom catalysts exhibited better activities than the single Pt single-atom catalyst, and their activities were better than that

of the supported Pt NPs catalyst. In addition, we compared the methanol oxidation activity with previous catalysts (Table S1), and found that the $T_{90\%}$ of Au₁Pt₁/meso-Fe₂O₃ (137 °C) was slightly higher than that of Mn₂O₃ @ δ-MnO₂ (119 °C) [35] and Pd/beta (110 °C) [36], but much lower than that of Au-ZnNb₂O₆ (200 °C) [37] and Pd/Al₂O₃ (200 °C) [36]. According to the calculated specific reaction rates and TOFs of the catalysts at 120 °C, it can be realized that specific reaction rate (224.17 $\mu\text{mol g}^{-1}\text{ noble metal s}^{-1}$) over Au₁Pt₁/meso-Fe₂O₃ was the biggest, which was slightly bigger than that (201.75 $\mu\text{mol g}^{-1}\text{ noble metal s}^{-1}$) over Pt₁/meso-Fe₂O₃, but much bigger than that (100.26 $\mu\text{mol g}^{-1}\text{ noble metal s}^{-1}$) over Pt_{np}/meso-Fe₂O₃. It can be seen from Fig. 1b that the specific reaction rate of the catalyst is consistent with the conversion rate. It is well known that the discrepancy in activation energy of the catalysts is reflected from their different activities. The E_a decreased in the sequence of meso-Fe₂O₃ (82 kJ mol⁻¹) > Pt_{np}/meso-Fe₂O₃ (44 kJ mol⁻¹) > Pt₁/meso-Fe₂O₃ (41 kJ mol⁻¹) > Au₁Pt₁/meso-Fe₂O₃ (36 kJ mol⁻¹) (Table 1), coinciding with the changing trend in activity of these catalysts. Compared with Pt₁/meso-Fe₂O₃, the partial replacement of Pt by Au (thus obtained the Au₁Pt₁/meso-Fe₂O₃ catalyst) effectively promoted the activity. The catalytic performance of the Au₁Pt₁/meso-Fe₂O₃ sample was further investigated in the presence of water. As shown in Fig. S3 and Table 1, the addition of 1.0 vol% H₂O did not decrease the methanol conversion, while the presence of 5.0 vol% H₂O made the methanol conversion decrease from 90% to 85% within 6 h. After water vapor was cut off, the catalytic activity could be well recovered.

To investigate the SO₂ resistance of the typical catalysts for methanol oxidation, we measured catalytic activities of Au₁Pt₁/meso-Fe₂O₃, Pt₁/meso-Fe₂O₃, and Pt_{np}/meso-Fe₂O₃ in the presence of 40 or 100 ppm SO₂, and the results are shown in Fig. 1c and d. When 40 ppm SO₂ was introduced for 6 h, methanol conversions over Au₁Pt₁/meso-Fe₂O₃ and

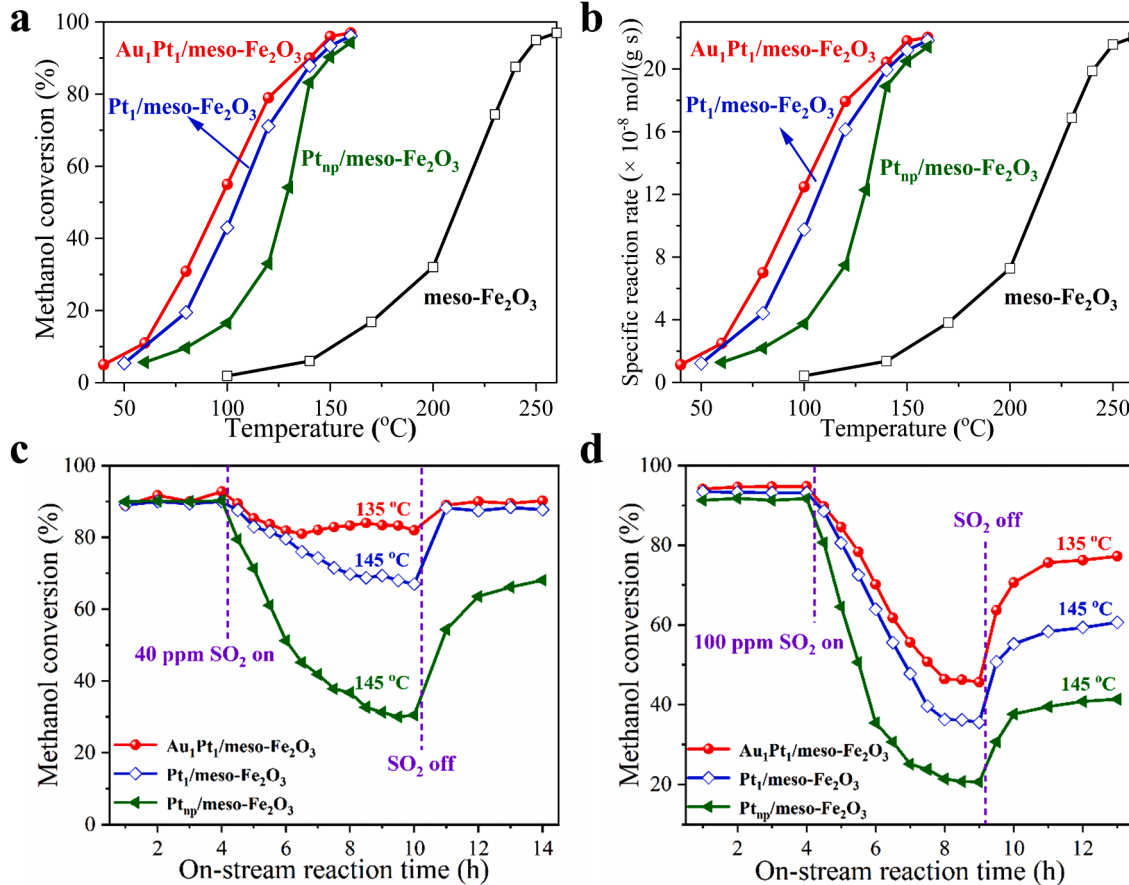


Fig. 1. Methanol conversion as a function of (a) temperature, (b) specific reaction rate and (c, d) on-stream reaction time over meso-Fe₂O₃, Pt_{np}/meso-Fe₂O₃, Pt₁/meso-Fe₂O₃, and Au₁Pt₁/meso-Fe₂O₃ in the presence of (c) 40 ppm SO₂ and (d) 100 ppm SO₂.

Table 1Catalytic activities, TOFs, specific reaction rates, and apparent activation energies (E_a) at $SV = 20\,000\,mL\,g^{-1}\,h^{-1}$, and noble metal dispersion of the catalysts.

Catalyst	Activity		Methanol combustion at 120 °C			E_a (kJ/mol)	Noble metal dispersion (%)
	$T_{50\%}$ (°C)	$T_{90\%}$ (°C)	TOF _{Noble metal} ($\times 10^{-2}\,s^{-1}$)	Specific reaction rate ($\mu\text{mol}/(\text{g}_{\text{Noble metal}}\,\text{s})$)	Specific reaction rate ($\times 10^{-2}\,\mu\text{mol}/(\text{g}_{\text{cat}}\,\text{s})$)		
meso-Fe ₂ O ₃	212	244	—	—	0.84	82	—
Pt _{np} /meso-Fe ₂ O ₃	128	148	5.90	100.26	9.03	44	24.5
Pt ₁ /meso-Fe ₂ O ₃	105	143	5.62	201.75	16.14	41	70.1
Au ₁ Pt ₁ /meso-Fe ₂ O ₃	96	137	6.51	224.17	17.94	36	67.5
Au ₁ Pt ₁ /meso-Fe ₂ O ₃ (5% H ₂ O)	98	148	6.13	211.16	16.90	—	—

Pt₁/meso-Fe₂O₃ were decreased to 82% and 68%, respectively, and gradually recovered after SO₂ was turned off. On the other hand, the methanol conversion over the Pt_{np}/meso-Fe₂O₃ catalyst decreased to 29%, and it was not recovered completely after SO₂ was cut off, indicating that the negative effect of low-concentration SO₂ on activity of the meso-Fe₂O₃-supported Au₁Pt₁ and Pt₁ single-atom catalysts was reversible, but that on activity of the supported Pt NPs catalyst was irreversible. This result suggests that the meso-Fe₂O₃-supported single-atom catalysts exhibited a better recovery ability. As shown in Fig. 1d, after introducing 100 ppm SO₂ for 5 h, the decrease of methanol conversion over each catalyst was higher than that caused by introducing 40 ppm SO₂, and the it was not fully recovered to the initial level after cutting off SO₂. However, Au₁Pt₁/meso-Fe₂O₃ showed the best activity recovery performance, and methanol conversion was gradually recovered to 75% within 3 h after SO₂ was cut off, while methanol conversions over Pt₁/meso-Fe₂O₃ and Pt_{np}/meso-Fe₂O₃ were recovered to 60% and 41%, respectively. In general, SO₂ resistance of the catalysts was in the order of Au₁Pt₁/meso-Fe₂O₃ > Pt₁/meso-Fe₂O₃ > Pt_{np}/meso-Fe₂O₃.

The SO₂ resistance of the above catalysts in benzene, CO and CH₄ oxidation was also measured. As shown in Fig. S4, the sequence of combustion activity and SO₂-resistant performance of the catalysts is Au₁Pt₁/meso-Fe₂O₃ > Pt₁/meso-Fe₂O₃ > Pt_{np}/meso-Fe₂O₃. Therefore, compared with the traditional supported Pt NPs catalysts, the meso-Fe₂O₃ supported AuPt bimetallic single-atom catalyst with the high SO₂ resistance has wide prospect in practical applications.

3.2. Physicochemical properties of the present catalysts

The actual noble metal contents measured by the ICP-AES technique are summarized in Table 2. The actual noble metal contents in Pt_{np}/meso-Fe₂O₃ and Pt₁/meso-Fe₂O₃ were 0.09 and 0.08 wt%, respectively, and the Au-Pt contents in Au₁Pt₁/meso-Fe₂O₃ were 0.02–0.06 wt%. The

Table 2Average crystallite sizes (D_c), BET surface areas, pore diameter, pore volumes, and actual metal loadings of the as-obtained catalysts.

Catalyst	D_c ^a (nm)	Surface area (m ² /g)	Pore diameter (nm)	Pore volume (cm ³ /g)	Actual Au loading ^b (wt%)	Actual Pt loading ^b (wt%)
meso-Fe ₂ O ₃	20.0	105.3	9.3	0.30	—	—
Pt _{np} /meso-Fe ₂ O ₃	21.3	105.8	9.3	0.29	—	0.09
Pt ₁ /meso-Fe ₂ O ₃	20.8	103.4	9.5	0.28	—	0.08
Au ₁ Pt ₁ /meso-Fe ₂ O ₃	21.1	103.3	9.8	0.29	0.02	0.06

^a Data were obtained according to the Scherrer equation using the FWHM of the (104) line of Fe₂O₃ in the XRD patterns;

^b Data were determined by the ICP-AES technique.

actual loadings of noble metals lower than the theoretical loadings might be due to that some Pt(NH₃)₄(NO₃)₂ and HAuCl₄ were not adsorbed and reduced during the catalyst preparation process. Fig. S5 shows the small- and wide-angle XRD patterns of the catalysts. In the small-angle XRD patterns, the recording of a diffraction signal at $2\theta = \text{ca. } 1^\circ$ indicates the formation of a three-dimensionally ordered mesoporous structure (meso-Fe₂O₃). As revealed in the wide-angle patterns, meso-Fe₂O₃ was of a rhombohedral crystal phase (JCPDS PDF# 33–0664). Since the Au and Pt were well dispersed on the surface of meso-Fe₂O₃ and their loadings were rather low, the crystal phases assignable to the noble metal phases were not detected. Fig. S6 represents the nitrogen adsorption–desorption isotherms and pore-size distributions of the catalysts. A type IV isotherm with an H1 hysteresis loop in the p/p_0 range of 0.4–0.9 suggests the presence of a uniform mesoporous architecture. As shown in Table 2, BET surface areas of the catalysts were in a range of 103–106 m²/g, and their average pore diameters and pore volumes were 9.3–9.8 nm and 0.28–0.30 cm³/g, respectively. Fig. 2 and Fig. S7 displays the HR-TEM and AC-HAADF-STEM images of Au₁Pt₁/meso-Fe₂O₃. The observations of a uniform ordered mesoporous structure were in consistent with the small-angle XRD and BET characterization results. Due to noble metals with high ordinal numbers often have a more pronounced contrast in the images, the luminous dots marked with the red circles in the images were regarded as the Au and Pt mixed atoms. We can observe from Fig. S8 that Pt NPs dispersed well on the surface of meso-Fe₂O₃, and the (111) crystal plane spacing of Pt was measured as 0.227 nm.

In situ CO-DRIFTS is a fast and convenient characterization technique to discriminate the Pt-group metal species (including metallic single atoms and NPs) in a supported noble metal catalyst [38]. Fig. S9 shows the CO-DRIFTS spectra of Au₁Pt₁/meso-Fe₂O₃ at 30 °C in different time. The broad absorption band at 2173 cm⁻¹ belonged to the gaseous CO adsorption, and the one at 2068 cm⁻¹ could correspond to the linear adsorption of CO on the surface Pt atom. The absorption band of CO on the Pt NPs was rigorously located at 2060 cm⁻¹ in the 0.25Pt_{np}/meso-Fe₂O₃ catalyst synthesized previously [34]. Single-atom catalysts often have different electrons from the NP catalysts due to the presence of special chemical bonds and active sites – the electronic structure could be altered with the change in coordination environment. Due to the different chemical potential energies, electrons are transferred from a single atom to the support through the chemical bond, resulting in a result that the single-atom often carries charges. Therefore, the absorption band of CO on the Pt single-atom displayed a blue shift owing to a positive charge, as compared with that on the Pt NPs [38,39].

3.3. Surface composition, redox property, and activation properties

Shown in Fig. S10 are Fe 2p, O 1s, Au 4f, and Pt 4f spectra of the catalysts, and their surface element compositions are summarized in Table 3. Fe 2p_{3/2} spectrum (Fig. S10a) of each catalyst could be decomposed into three components: the one at binding energy (BE) = 712.5 eV was ascribed to the surface Fe³⁺ species, and the one at BE = 710.5 eV together with the satellite at BE = 717.8 eV was assigned to

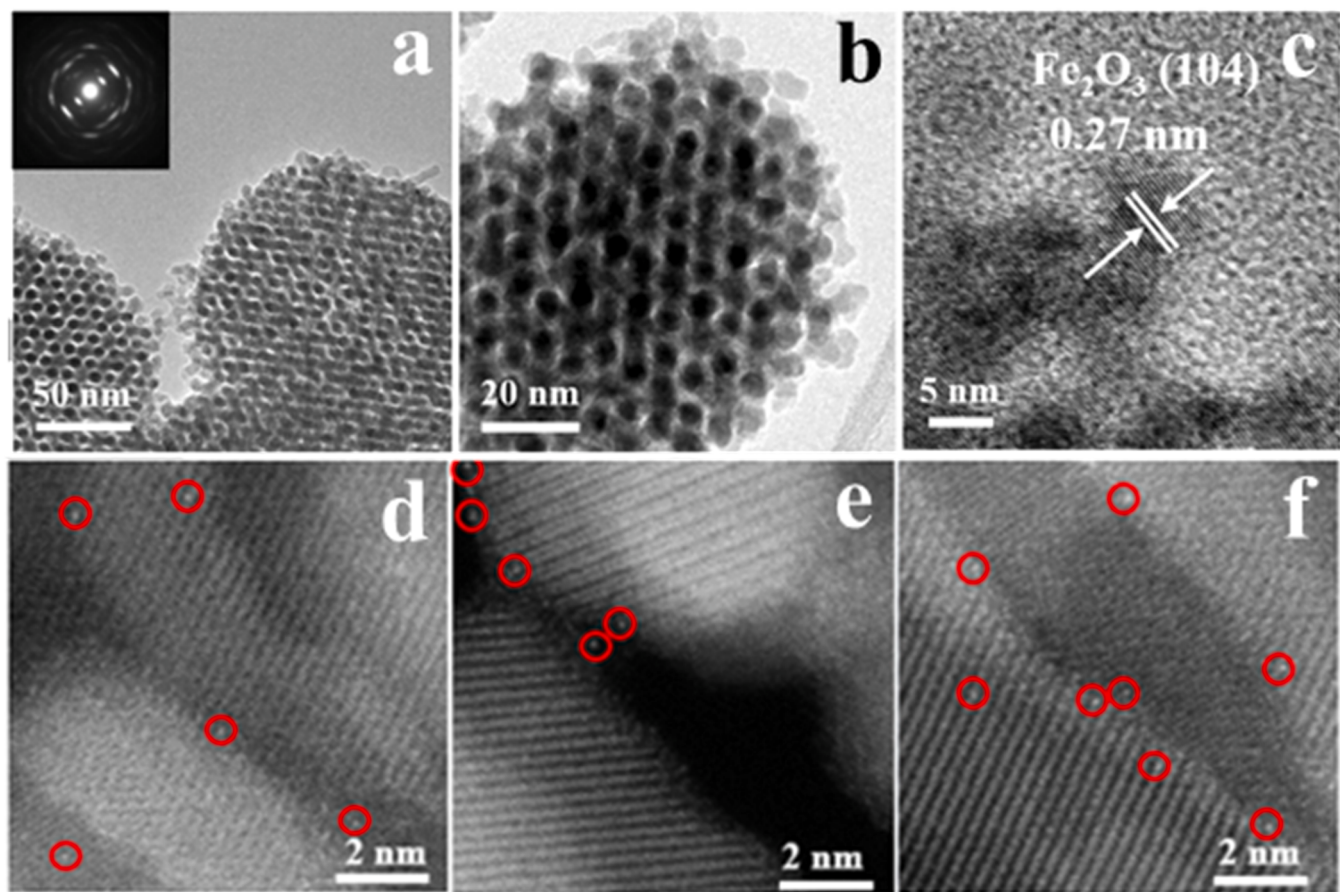


Fig. 2. (a–c) HR-TEM images and (d–f) AC-HAADF-STEM images of the $\text{Au}_1\text{Pt}_1/\text{meso-Fe}_2\text{O}_3$ catalyst.

Table 3
Surface element compositions, H_2 consumption, O_2 desorption, and methanol desorption of the catalysts.

Catalyst	Surface element composition ^a			O_2 desorption ^c		H_2 consumption ^b (mmol/g)	Methanol desorption ^d (mol/g)
	$\text{Fe}^{2+}/\text{Fe}^{3+}$ molar ratio	$\text{O}_{\text{ads}}/\text{O}_{\text{latt}}$ molar ratio	$\text{Au}^0/\text{Au}^{\delta+}$ molar ratio	O_{ads} (mmol/g)	O_{latt} (mmol/g)		
meso- Fe_2O_3	0.75	0.36	–	–	3.09	16.3	0.54
$\text{Au}_1\text{Pt}_1/\text{meso-Fe}_2\text{O}_3$	0.92	0.68	0.18	1.88	6.49	17.6	1.21
$\text{Pt}_1/\text{meso-Fe}_2\text{O}_3$	0.87	0.49	–	1.75	5.37	17.5	1.09
$\text{Pt}_{\text{np}}/\text{meso-Fe}_2\text{O}_3$	0.82	0.45		0.95	4.28	17.2	1.05

^a Data were estimated by quantitatively analyzing the XPS spectra of the catalysts;

^b Data were estimated by quantitatively analyzing the H_2 -TPR profiles;

^c Data were calculated by quantitatively analyzing the O_2 -TPD profiles of the catalysts;

^d Data were calculated by quantitatively analyzing the Methanol-TPD profiles of the catalysts.

the surface Fe^{2+} species [34]. O 1 s spectrum (Fig. S10b) of each catalyst could be deconvoluted into three components at BE = 529.8, 531.4, and 533.1 eV, assignable to the surface lattice oxygen (O_{latt}), adsorbed oxygen (O_{ads} , e.g., O^{2-} , O_2^{2-} or O^-), and adsorbed water or carbonate species, respectively. As shown in Table 3, the surface $\text{Fe}^{2+}/\text{Fe}^{3+}$ and $\text{O}_{\text{ads}}/\text{O}_{\text{latt}}$ molar ratios on meso- Fe_2O_3 increased from 0.75 and 0.36–0.83–0.92 and 0.47–0.52 after loading of the noble metal, respectively. It is indicated that there was electron transfer between the noble metal and the support. The $\text{Au}_1\text{Pt}_1/\text{meso-Fe}_2\text{O}_3$ catalyst with the best activity possessed the highest surface Fe^{2+} and O_{ads} concentrations, indicating there was a strong interaction between the noble metal single atoms and the Fe_2O_3 support. Loading of Au–Pt promoted the increase in amount of surface oxygen vacancies, thus forming a more amount of surface adsorbed oxygen species and further making a contribution to methanol oxidation. Au 4 f spectrum (Fig. S10c) of each catalyst could

be decomposed into two groups of doublets: the components at BE = 74.0 and 87.7 eV were attributed to the surface metallic Au (Au^0) species, while the ones at BE = 85.2 and 88.8 eV were ascribed to the surface $\text{Au}^{\delta+}$ species [40]. Due to the calcination treatment, no Pt 4 f XPS signal at BE = 71.0 eV of each catalyst assignable to the surface metallic Pt (Pt^0) species was recorded (Fig. S10d), which indicates that most of the surface Pt species on the above catalysts were in an oxidized state. The difference in the valence state leads to the displacement of Pt 4 f binding energy. The surface Pt species was mainly present in the form of Pt–O–Fe bonds (i.e., Pt^{2+} at BE = 73.6 eV) on the $\text{Au}_1\text{Pt}_1/\text{meso-Fe}_2\text{O}_3$ and $\text{Pt}_1/\text{meso-Fe}_2\text{O}_3$ catalysts, but it was mainly present in the form of PtO_2 (i.e., Pt^{4+} at BE = 73.6 eV) on the $\text{Pt}_{\text{np}}/\text{meso-Fe}_2\text{O}_3$ catalyst [41].

Redox property and methanol adsorption capacity of the typical catalysts were investigated by the techniques of H_2 -TPR, O_2 -TPD,

Methanol-TPD, and Methanol-TPO. The reducibility and metal–support interactions of the catalysts were studied using the H₂-TPR technique (Fig. 3a). In Fig. 3a, the peaks at 80–120 °C were attributed to the reduction of oxidized Au^{δ+} or Pt^{δ+} to Au⁰ or Pt⁰, the peaks at 120–375 °C were attributed to the reduction of Fe₂O₃ to Fe₃O₄, and the peaks above 375 °C were ascribed to the reduction of Fe_{Ox} to Fe⁰ [34,42]. The reduction peaks of noble metals in these catalysts were not detected, due to their low loadings. Compared with Pt_{np}/meso-Fe₂O₃, the first reduction peak of Pt₁/meso-Fe₂O₃ and Au₁Pt₁/meso-Fe₂O₃ was moved to a lower temperature, which was due to the assisted reduction of iron oxide by the spillover hydrogen from the reduced Au and/or Pt. The more the spillover hydrogen, the stronger the metal–support interaction [43]. The first reduction peak temperature of the Au₁Pt₁/meso-Fe₂O₃ catalyst was the lowest, which indicates that there was the strongest interaction between the noble metal single atoms and the Fe₂O₃ support.

Oxygen adsorption and activation properties of the catalysts were investigated by the O₂-TPD technique. We use the MS signal to accurately identify the desorbed O₂ (*m/z* = 32). In the O₂-TPD profile (Fig. 3b), the peaks in the range of 50–250 °C for each catalyst were mainly ascribed to desorption of adsorbed oxygen species, and the wide peaks higher than 280 °C were ascribed to the desorption of lattice oxygen species [44]. The oxygen desorption amount on the meso-Fe₂O₃ catalyst significantly increased after the loading of noble metals on meso-Fe₂O₃. Among these catalysts, Au₁Pt₁/meso-Fe₂O₃ exhibited the highest adsorption and lattice oxygen desorption amounts of 1.88 and 6.49 mmol g⁻¹, respectively, indicating that it possessed good oxygen adsorption and activation ability.

The ability of low-temperature VOCs adsorption and desorption of a

catalyst is a vital factor for its catalytic activity. We studied methanol adsorption behaviors of the samples by the Methanol-TPD technique (Fig. 3c). The temperature of methanol desorption on each catalyst was below 320 °C. The peaks at 90–103 °C were ascribable to the desorption of weakly adsorbed methanol, and the peaks in the range of 240–282 °C were ascribable to the desorption of strongly adsorbed methanol. The methanol desorption peak was shifted to a lower temperature after loading of noble metals, suggesting that the strong interaction between Pt or Au–Pt and meso-Fe₂O₃ was beneficial for the adsorption of methanol. Previously, we found that VOC adsorption capacity of a catalyst played a priority role in governing the catalytic activity, as compared with the oxygen adsorption capacity [45]. The amount of methanol desorption was highly associated with the catalytic activity.

The methanol desorption behaviors at room temperature of the Au₁Pt₁/meso-Fe₂O₃ and Pt_{np}/meso-Fe₂O₃ catalysts were investigated by the in situ DRIFTS technique, and the results are shown in Fig. S11. In the in situ DRIFTS spectra of both catalysts, the bands at 2970, 1457, and 1244 cm⁻¹ were attributed to the surface-bound hydroxyl species, and the ones at 2862 and 1031 cm⁻¹ were ascribed to the vibration of the C–H bond and methoxy species, respectively. As the purge time increased, these bands were gradually weakened in intensity, suggesting that the chemically adsorbed species were left on the surface of the catalyst after the physically adsorbed species were desorbed. In the saturated state of adsorption at 25 °C, the appearance of CO₂ adsorption peaks (2331 cm⁻¹ and 2368 cm⁻¹) indicated that methanol oxidation was easy to occur on supported Pt-based catalysts.

In order to further investigate the methanol activation ability of the typical catalysts at 50–700 °C, we carried out the Methanol-TPO

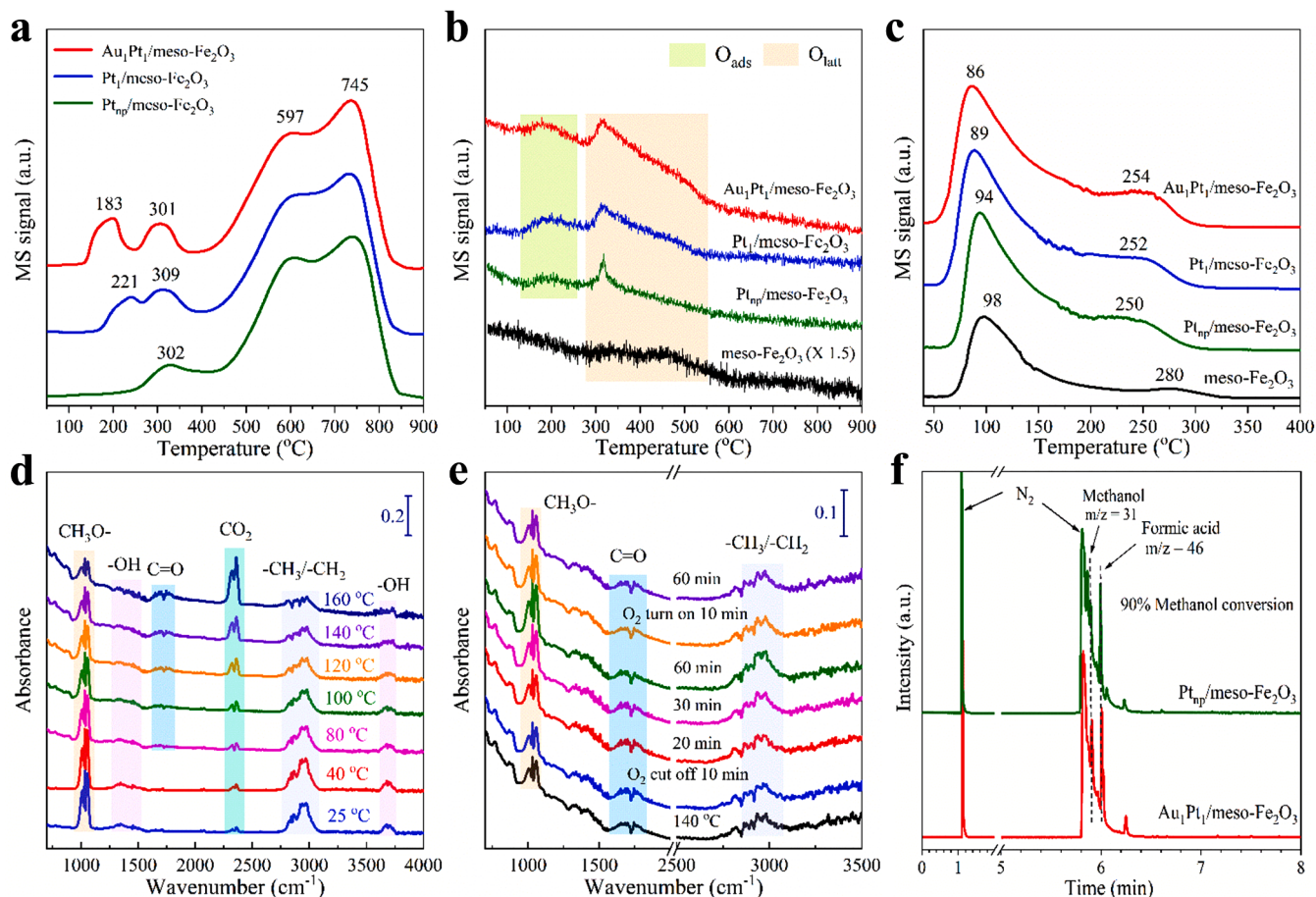


Fig. 3. (a) H₂-TPR, (b) O₂-TPD, and (c) Methanol-TPD profiles of meso-Fe₂O₃, Pt_{np}/meso-Fe₂O₃, Pt₁/meso-Fe₂O₃, and Au₁Pt₁/meso-Fe₂O₃, (d, e) in situ DRIFTS spectra of methanol oxidation over Au₁Pt₁/meso-Fe₂O₃, and (f) GC/MS chromatograms of the gaseous organic products at a methanol conversion of 90% over Au₁Pt₁/meso-Fe₂O₃ and Pt_{np}/meso-Fe₂O₃.

experiments. As shown in Fig. S12, the main reaction products were H_2O and CO_2 . Most of the methanol on the surface of the catalysts were desorbed at low temperatures ($< 200^\circ\text{C}$), which were attributed to the desorption of physically or weakly chemically adsorbed methanol. In the H_2O and CO_2 signals, the peaks below 200°C were ascribed to the reaction between the above physically or weakly chemically adsorbed methanol and oxygen species, and the ones in the range of $200\text{--}300^\circ\text{C}$ could be ascribed to assigned to the reaction between the strongly chemically adsorbed methanol and the adsorbed oxygen species. In addition, the peaks above 300°C were attributed to the reaction between the strongly chemically adsorbed methanol and lattice oxygen species. It is observed that the temperatures of the CO_2 and H_2O peaks of the $\text{Au}_1\text{Pt}_1/\text{meso-Fe}_2\text{O}_3$ catalyst were lower than that of the $\text{Pt}_{\text{np}}/\text{meso-Fe}_2\text{O}_3$ catalyst, corresponding to the good low-temperature catalytic activity.

3.4. Reaction pathway for methanol removal

The intermediate distributions in the methanol oxidation process were recorded the in situ DRIFTS spectra of the catalysts (Fig. 3d). The bands regarding the surface methoxy species (at 1031 cm^{-1}), $-\text{OH}$ (at $3687, 1344$, and 1457 cm^{-1}), and C-H bond (at 2862 and 2970 cm^{-1}) were observed at the initial temperature. When the temperature rose, a new band at 1715 cm^{-1} appeared, which corresponded to the symmetric carbonyl groups ($\text{C}=\text{O}$), i.e., the formation of the formaldehyde intermediate [46]. Moreover, formic acid was detected as an intermediate in an online GC/MS analysis when methanol conversion reached 90% (Fig. 3f). Interestingly, the characteristic bands of formic acid were not detected in the in situ DRIFTS spectrum, suggesting that formic acid was an unstable intermediate and easily decomposed. With the rise in temperature, the intensity of the band assignable to the methoxy species gradually decreased, while that of the band attributable to the CO_2 species gradually increased. Jiang et al. [47] also reported the mechanism of methanol oxidation at an atomic level over the $\text{Pt}_1/\text{Co}_3\text{O}_4$ catalyst using the ^{18}O isotope tracing technique and DFT calculation. The possible reaction pathways were that the CH_3OH and O_2 were firstly adsorbed on the catalyst surface, then the $-\text{OH}$ group in CH_3OH was dissociated, leading to formation of the Au-methoxy or Pt-methoxy species. With the assistance of the regeneration of the active oxygen vacancies and electron transfer between Au or Pt atoms and Fe_2O_3 , the C-H bonds in the methoxy species were activated and cleaved, giving rise to the generation of the formaldehyde (CH_2O) species as an intermediate. Then, the formed formaldehyde intermediate was converted to formic acid, which was quickly oxidized into H_2O and CO_2 . In brief, methanol oxidation over the present samples might follow a pathway of methanol \rightarrow methoxy species \rightarrow formaldehyde \rightarrow formic acid \rightarrow CO_2 and H_2O .

It is widely accepted that the Langmuir–Hinshelwood (L–H) and Mars–van Krevelen (MvK) mechanisms can well explain the oxidation of most of VOCs over the catalysts [48,49]. The key issue involving in the rate-limiting step of the L–H mechanism was the adsorption capacity of oxygen and organic reactants. The MvK mechanism involved an oxidation–reduction recycle on the surface of the catalyst: VOCs were first oxidized by the active oxygen species adsorbed on the surface of the catalyst, then the active oxygen species were regenerative via the activation of gas-phase O_2 . The regeneration of the surface adsorbed active oxygen species was strongly linked to the redox ability of the catalyst, which was deeply influenced by the noble metal–support interaction. It was reported in the literature that the MvK mechanism was suitable for VOCs oxidation over the metal oxides and their supported Pt catalysts under the oxygen-rich conditions [50–52]. As shown in Fig. 3e, under the same reaction conditions as the activity evaluation, O_2 was cut off at 140°C and the in situ DRIFTS spectra was recorded at different times. The peak strength of the reaction intermediates increased slightly and remained stable within 1 h after O_2 was cut off, and gradually weakened after O_2 was re-introduced. In other words, the catalytic activity

decreases after oxygen was cut off, but the catalyst was not completely deactivated, indicating that lattice oxygen was also involved in methanol oxidation reaction, especially at high temperature. According to the above investigation results, we can realize that methanol oxidation over the meso- Fe_2O_3 -supported bimetallic Au_1Pt_1 catalysts studied in the present work follow the MvK mechanism. In addition, the activation and cleavage of first C–H bond in methoxy species adsorbed on the surface of noble metal is assisted by the electron transfers between the noble metals and the support, that is, the strong metal-support interactions (SMSI) [47].

3.5. Insight into SO_2 resistance mechanism

In order to explain why the meso- Fe_2O_3 supported Au_1Pt_1 catalyst showed much better SO_2 resistance than the supported Pt_1 catalyst, and they also better than the supported Pt_{np} catalyst, a series of the related characterization analysis were carried out. The catalysts after the SO_2 resistance test were denoted as $\text{Au}_1\text{Pt}_1/\text{meso-Fe}_2\text{O}_3\text{-U}$, $\text{Pt}_1/\text{meso-Fe}_2\text{O}_3\text{-U}$ and $\text{Pt}_{\text{np}}/\text{meso-Fe}_2\text{O}_3\text{-U}$, respectively.

As shown in the FT-IR spectra (Fig. S13), the bands at $1219, 1145, 1045$, and 1035 cm^{-1} corresponding to the surface sulfate and/or sulfite species were recorded on the catalysts after the SO_2 resistance test, indicating that the sulfates that were difficult to decompose were deposited on both catalysts [38]. In order to investigate the sulfate deposition behavior on each catalyst, 5 h of 40 ppm SO_2 -aging treatment was carried out when methanol conversion was around 90%, and the He-TPD technique was applied to measure the SO_2 signal generated by the high-temperature sulfate decomposition. As shown in Fig. 4a, there were two SO_2 desorption peaks: The first peak at the lower temperature was attributed to desorption of the weakly bonded sulfates, while the second peak was attributed to desorption of the strongly bonded sulfates [53]. It can be observed that intensity of the first peak for the three catalysts was higher than that of the second peak, suggesting that the weakly bonded sulfate species deposited mainly on the catalyst surface after 5 h of SO_2 -aging treatment. We observed that the amount of sulfate desorption decreased in the order of $\text{Au}_1\text{Pt}_1/\text{meso-Fe}_2\text{O}_3\text{-U} > \text{Pt}_1/\text{meso-Fe}_2\text{O}_3\text{-U} > \text{Pt}_{\text{np}}/\text{meso-Fe}_2\text{O}_3\text{-U}$, indicating that the supported single atom catalysts exhibited stronger sulfate decomposition ability. It also shows that the single atoms were more effective for preventing deactivation due to sulfur poisoning. Moreover, sulfur contents in the catalysts after the reaction were obtained from the quantitative analysis of Fig. 4a, and the results were added to Table S2. As shown in Table S2, the amounts of SO_2 desorption from $\text{Au}_1\text{Pt}_1/\text{meso-Fe}_2\text{O}_3\text{-U}$, $\text{Pt}_1/\text{meso-Fe}_2\text{O}_3\text{-U}$, and $\text{Pt}_{\text{np}}/\text{meso-Fe}_2\text{O}_3\text{-U}$ were $126, 77$, and $65\text{ }\mu\text{mol/g}$, respectively.

The S 2p, O 1s and Fe 2p XPS spectra of the samples after the SO_2 -resistant test are shown in Fig. 4b–c and S14, and their $\text{S}^{6+}/(\text{S}^{4+} + \text{S}^{6+})$, $\text{O}_{\text{ads}}/\text{O}_{\text{latt}}$, and $\text{Fe}^{2+}/\text{Fe}^{3+}$ molar ratios are summarized in Table S2. There was a slight drop in $\text{O}_{\text{ads}}/\text{O}_{\text{latt}}$ ratio of the catalysts after exposure to SO_2 . The result reveals that SO_2 poisoning would reduce amount of the O_{ads} species. However, the decrease degree of the $\text{O}_{\text{ads}}/\text{O}_{\text{latt}}$ ratio on each catalyst was almost the same. Therefore, the effect of SO_2 on the oxygen adsorption species of the catalysts was weak, i.e., such an effect was not the main factor governing activity of the catalyst. Two different surface sulfur-bearing species were identified in the S 2p XPS spectra (Fig. 4b). The doublets at BE = 168.4 and 169.6 eV as well as 168.9 and 170.0 eV could be assignable to the $2\text{p}_{3/2}$ and $2\text{p}_{1/2}$ final states of the surface S^{4+} as well as S^{6+} species, respectively [45]. The surface S^{4+} species corresponded to the formation of sulfite (SO_3^{2-}) via the adsorption of SO_2 , whereas the surface S^{6+} species were due to the formation of sulfate (SO_4^{2-}) via oxidation of SO_2 over the catalyst [54]. The $\text{S}^{6+}/(\text{S}^{4+} + \text{S}^{6+})$ molar ratio on $\text{Au}_1\text{Pt}_1/\text{meso-Fe}_2\text{O}_3\text{-U}$ was calculated to be the highest, suggesting that a more amount of sulfate deposited on this catalyst. The result indicates that SO_2 was prone to be oxidized over meso- Fe_2O_3 to form the iron sulfate species (FeSO_4 or $\text{Fe}_2(\text{SO}_4)_3$) on the $\text{Au}_1\text{Pt}_1/\text{meso-Fe}_2\text{O}_3$ catalyst in the same SO_2 -containing atmosphere.

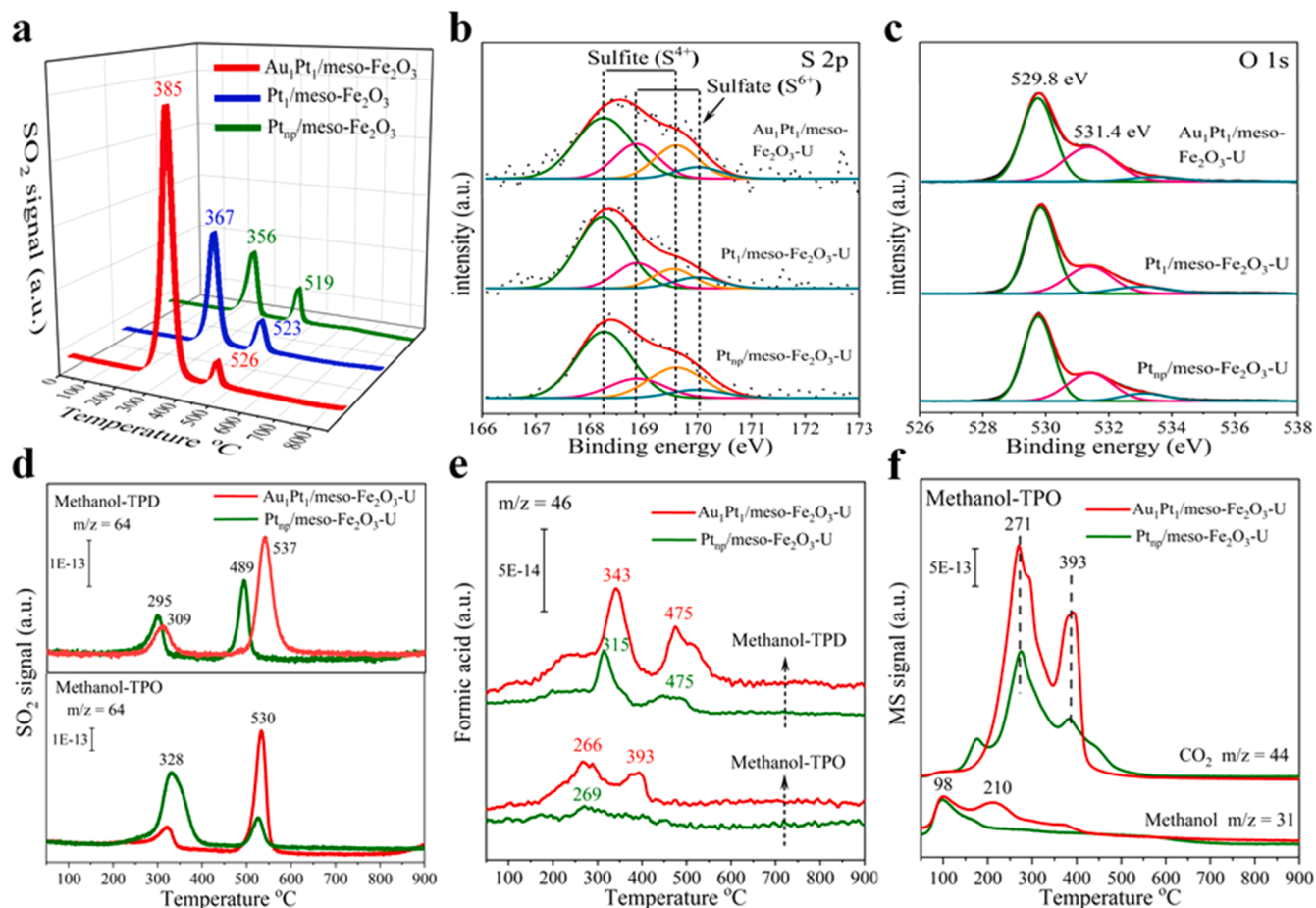


Fig. 4. (a) SO_2 desorption in the He-TPD profiles of the catalysts after 40 ppm SO_2 -aging treatment at a 90% methanol conversion for 5 h, (b, c) XPS spectra of the catalysts after SO_2 -resistance test, (d) SO_2 and (e) formic acid desorption in the Methanol-TPD/TPO profiles of the catalysts after SO_2 -resistance test, and (f) Methanol-TPO profiles of the $\text{Au}_1\text{Pt}_1/\text{meso-Fe}_2\text{O}_3$ and $\text{Pt}_{\text{np}}/\text{meso-Fe}_2\text{O}_3$ catalysts after SO_2 -resistance test.

Fig. 4d shows the SO_2 desorption signals in Methanol-TPD and Methanol-TPO profiles of $\text{Au}_1\text{Pt}_1/\text{meso-Fe}_2\text{O}_3\text{-U}$ and $\text{Pt}_{\text{np}}/\text{meso-Fe}_2\text{O}_3\text{-U}$. Different from the He-TPD results, the proportion of the strongly bonded sulfates in $\text{Au}_1\text{Pt}_1/\text{meso-Fe}_2\text{O}_3\text{-U}$ was much higher than that of the weakly bonded sulfates, suggesting that the unstable sulfite species were gradually transformed into the stable sulfate species after a long

time reaction in the atmosphere containing methanol and SO_2 . It is reasonable to assume that the stable sulfate species were mainly ferric sulfate, and in terms of desorption amount more sulfates were deposited on $\text{Au}_1\text{Pt}_1/\text{meso-Fe}_2\text{O}_3\text{-U}$ than on $\text{Pt}_{\text{np}}/\text{meso-Fe}_2\text{O}_3\text{-U}$. In addition, the signal of formic acid as an intermediate was detected ($m/z = 46$). As shown in Fig. 4e, no matter in Methanol-TPD or Methanol-TPO profiles,

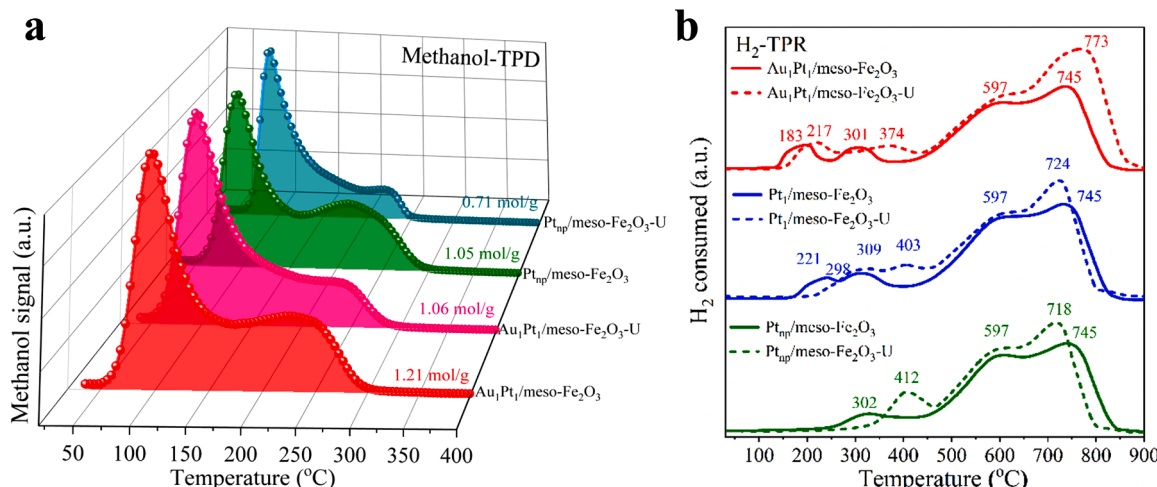


Fig. 5. (a) Methanol desorption in the Methanol-TPD and (b) H_2 -TPR profiles of fresh $\text{Au}_1\text{Pt}_1/\text{meso-Fe}_2\text{O}_3$, $\text{Pt}_1/\text{meso-Fe}_2\text{O}_3$, $\text{Pt}_{\text{np}}/\text{meso-Fe}_2\text{O}_3$ and the catalyst after SO_2 -resistance test.

the amount of formic acid desorption from $\text{Au}_1\text{Pt}_1/\text{meso-Fe}_2\text{O}_3\text{-U}$ was significantly higher than that from $\text{Pt}_{\text{np}}/\text{meso-Fe}_2\text{O}_3\text{-U}$, indicating that more formic acid was formed on $\text{Au}_1\text{Pt}_1/\text{meso-Fe}_2\text{O}_3$ in the SO_2 atmosphere. Fig. 4f shows the signal of methanol and CO_2 desorption in Methanol-TPO profiles. Compared with the fresh catalyst, the methanol desorption amount on both catalysts decreased. Moreover, the CO_2 production amount on $\text{Pt}_{\text{np}}/\text{meso-Fe}_2\text{O}_3\text{-U}$ were much lower than those on $\text{Au}_1\text{Pt}_1/\text{meso-Fe}_2\text{O}_3\text{-U}$, suggesting that the deactivation caused by SO_2 of $\text{Pt}_{\text{np}}/\text{meso-Fe}_2\text{O}_3$ was more serious, while that of $\text{Au}_1\text{Pt}_1/\text{meso-Fe}_2\text{O}_3$ was much less, which was also in line with the change trend in SO_2 -resistant activity.

The methanol adsorption behaviors over $\text{Au}_1\text{Pt}_1/\text{meso-Fe}_2\text{O}_3\text{-U}$ and $\text{Pt}_{\text{np}}/\text{meso-Fe}_2\text{O}_3\text{-U}$ are shown in Fig. 5a. After SO_2 poisoning, the amount of methanol desorption over the $\text{Au}_1\text{Pt}_1/\text{meso-Fe}_2\text{O}_3$ catalyst decreased slightly from 1.21 to 1.06 mol g^{-1} , while that of $\text{Pt}_{\text{np}}/\text{meso-Fe}_2\text{O}_3$ decreased significantly from 1.05 to 0.71 mol g^{-1} . The adsorption capacity of methanol is directly related to the active noble metals. Therefore, it indicated that SO_2 poisoning would weaken the methanol adsorption capacity, and a greater effect was observed over the supported Pt NPs catalyst, than the supported Au–Pt single-atom catalyst. In other words, Au–Pt single atoms show better resistance to SO_2 poisoning. To further investigate the effect of SO_2 on the supported noble metals, we also compared the $\text{H}_2\text{-TPR}$ profiles of fresh $\text{Au}_1\text{Pt}_1/\text{meso-Fe}_2\text{O}_3$, $\text{Pt}_1/\text{meso-Fe}_2\text{O}_3$, and $\text{Pt}_{\text{np}}/\text{meso-Fe}_2\text{O}_3$ and their corresponding samples after the SO_2 resistance test. As shown in Fig. 5b, the last peak (corresponding to reduction of bulk lattice oxygen in Fe_2O_3) of $\text{Au}_1\text{Pt}_1/\text{meso-Fe}_2\text{O}_3\text{-U}$ shifted towards high temperature, while that of the other two catalysts was moved to a lower temperature. This result suggests that the lattice oxygen in Fe_2O_3 was more difficult to be reduced after $\text{Au}_1\text{Pt}_1/\text{meso-Fe}_2\text{O}_3$ was treated in SO_2 , which might be caused by the further reaction between SO_2 or sulfite and lattice oxygen in Fe_2O_3 to generate ferric sulfate (which was difficult to decompose). The shift of the peak below 370 °C was directly related to catalytic activity of the supported noble metals. As can be seen from the profiles, these peaks of all the catalysts were shifted to the higher temperatures, suggesting that catalytic activity of the noble metal decreased. Meanwhile, the shift degree of $\text{Au}_1\text{Pt}_1/\text{meso-Fe}_2\text{O}_3$ was the least, suggesting that SO_2 had the weakest toxicity to Au_1Pt_1 . On the other hand, it had the strongest toxicity to Pt_{np} . Combined with the He-TPD results of the samples after SO_2 -aging treatment, it was found that Au_1Pt_1 exhibited the strongest decomposition ability of sulfite and/or sulfate species.

It can be seen from the reduction and methanol adsorption performance of the fresh catalysts and the catalysts after reaction that the activity of catalysts for methanol oxidation is directly related to the activity of noble metal active sites. The stronger the sulfate-decomposition ability of the noble metal active sites, the less easily it is poisoned, and the more SO_2 spilt from its surface. The spillover SO_2 tends to react with the meso- Fe_2O_3 to form ferric sulfate. In this catalytic system, the meso- Fe_2O_3 support played the role of a sacrificial site to store SO_2 , so the main sulfate deposited in the catalyst was ferric sulfate. Therefore, compared with the supported Pt NPs catalyst, although more ferric sulfate was generated in the supported single atom catalysts, the noble metal active sites poisoning was less, causing it to exhibit better performance under the sulfur environment.

In order to probe the SO_2 resistance mechanism, it is necessary to clarify the pathway of catalytic methanol oxidation in the absence or presence of SO_2 , and the in situ DRIFTS spectra (Fig. 6) of the transient reactions between SO_2 and adsorbed species (methanol + O_2) over $\text{Au}_1\text{Pt}_1/\text{meso-Fe}_2\text{O}_3$ and $\text{Pt}_{\text{np}}/\text{meso-Fe}_2\text{O}_3$ at 140 and 160 °C were recorded, respectively. After 1 h of SO_2 introduction, the characteristic bands of formic acid (1726, 1448, 1270, and 1120 cm^{-1} corresponded to the surface C=O , $-\text{COO}$, and C-O , respectively) appeared on the $\text{Au}_1\text{Pt}_1/\text{meso-Fe}_2\text{O}_3$ catalyst (Fig. 6a). The newly emerged band at 1377 cm^{-1} on $\text{Au}_1\text{Pt}_1/\text{meso-Fe}_2\text{O}_3$ was ascribed to the asymmetric stretching frequency of the S=O=S bond assignable to the sulfate species adsorbed on iron oxide [55]. Intensity of the bands due to formic acid was gradually increased with the extension of SO_2 addition, but it was gradually declined after SO_2 was cut off. These results indicate that SO_2 was more inclined to react with meso- Fe_2O_3 to form the iron sulfate species, resulting in accumulation of formic acid during the reaction process in the presence of SO_2 . However, formic acid was not detected on $\text{Pt}_{\text{np}}/\text{meso-Fe}_2\text{O}_3$ (Fig. 6b). Intensity of the band due to the adsorbed methoxy species was gradually increased after SO_2 was turned on, implying that methanol oxidation activity decreased and the activity could not be restored by turning off SO_2 . This result was consistent with the rapid drop in activity within 3 h of SO_2 introduction over the $\text{Pt}_{\text{np}}/\text{meso-Fe}_2\text{O}_3$ catalyst. The online GC/MS analysis technique was used to further reveal the changes of reaction intermediates in the SO_2 -resistance tests (Fig. 7). After SO_2 was introduced, the amount of formic acid on $\text{Au}_1\text{Pt}_1/\text{meso-Fe}_2\text{O}_3$ was increased compared with that on $\text{Pt}_{\text{np}}/\text{meso-Fe}_2\text{O}_3$ (Fig. 7a and b). However, $I_{\text{formic acid}}/I_{\text{methanol}}$ greatly increased from 0.79 to 24.00 over meso- Fe_2O_3 due to the SO_2

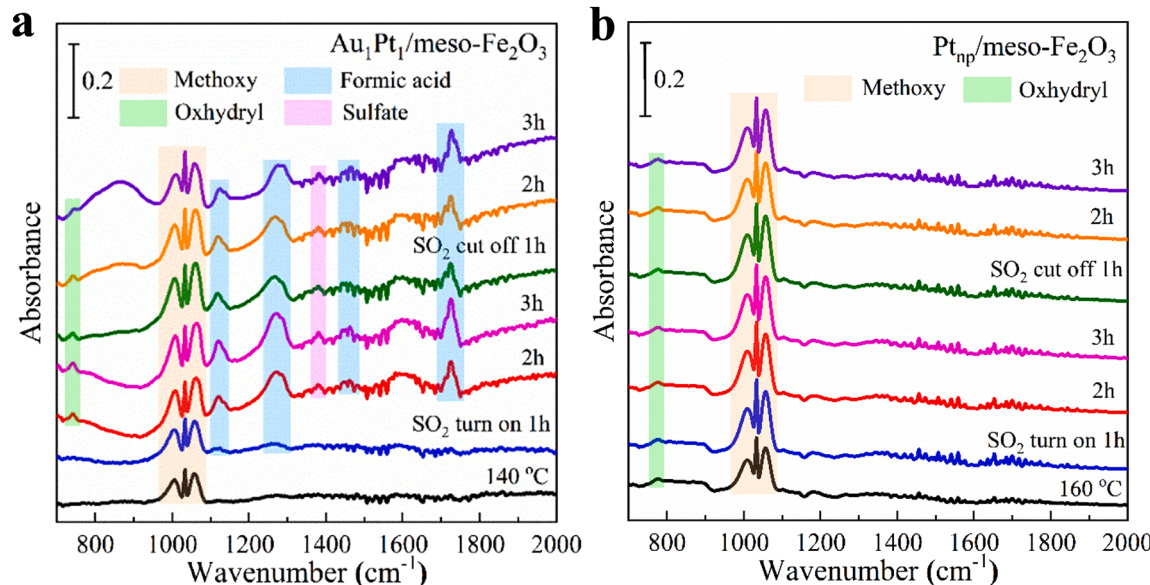


Fig. 6. *In situ* DRIFTS spectra under the conditions same as those adopted in catalytic activity evaluation.

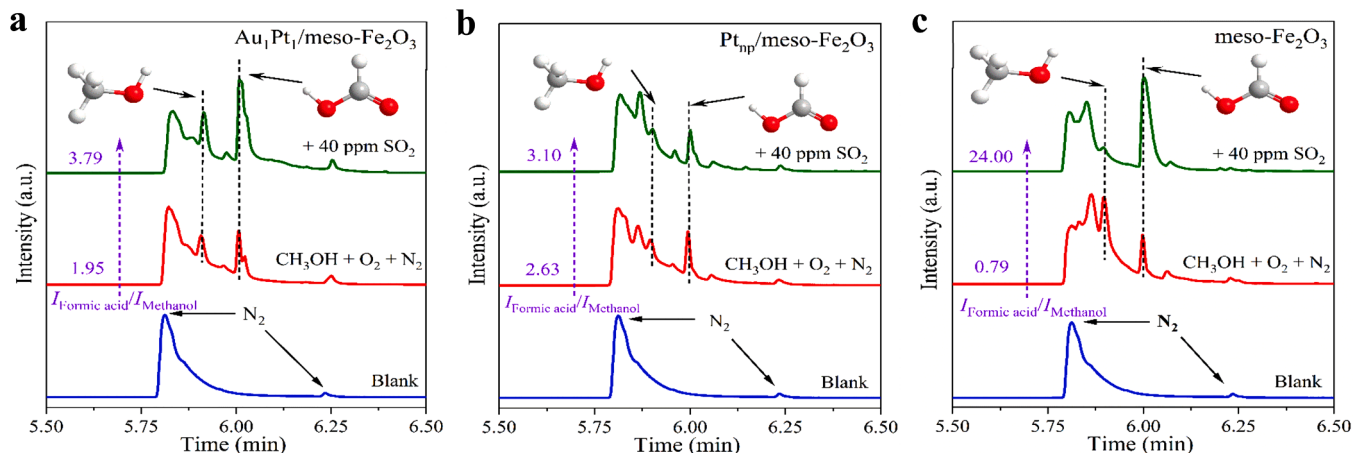


Fig. 7. GC/MS chromatograms of the gaseous organic products at a 90% methanol conversion in the absence or presence of 40 ppm SO_2 .

introduction, indicating that the formation of sulfates on meso- Fe_2O_3 lead to a large accumulation of formic acid. Moreover, the amount of formic acid also increased after the introduction of SO_2 over $\text{Pt}/\text{meso-Fe}_2\text{O}_3$ catalyst (Fig. S15). It confirmed that the deposition of iron sulfates was highly related to the accumulation of formic acid.

Combining the above characterization results and the literature analysis, we propose the methanol oxidation mechanism in the presence of SO_2 over the $\text{Au}_1\text{Pt}_1/\text{meso-Fe}_2\text{O}_3$ and $\text{Pt}_{\text{np}}/\text{meso-Fe}_2\text{O}_3$ catalysts, as illustrated in Fig. 8. For $\text{Au}_1\text{Pt}_1/\text{meso-Fe}_2\text{O}_3$, the Au-Pt bimetal single-atom site played a strong role in sulfate decomposition and showed a strong regeneration ability, SO_2 in the atmosphere was preferentially adsorbed on the meso- Fe_2O_3 support to generate the sulfites, which were then transformed into the stable sulfates (FeSO_4 or $\text{Fe}_2(\text{SO}_4)_3$) via the deep oxidation with the lattice oxygen species. In the reaction pathway, the dissociation of $-\text{OH}$ group in CH_3OH led to generation of the Au-methoxy and Pt-methoxy species. Since it was not poisoned, the

strong metal-support interaction at the interface proceeded smoothly, promoting cleavage of the first C-H bond in the methoxy species to generate formaldehyde, which is a significant step for methanol oxidation [56–58]. Then, a large number of sulfates were deposited on Fe_2O_3 , resulting in the accumulation of formic acid during the reaction process. Therefore, it is reasonable to assume that in the last step of the reaction (rapid conversion of formic acid into CO_2 and H_2O), in addition to the adsorbed oxygen species, the lattice oxygen in Fe_2O_3 also participated in the reaction. As part of Fe_2O_3 was converted into ferric sulfate, the reduction of lattice oxygen activity slowed down the reaction at this step, leading to the accumulation of formic acid, but with the assistance of the adsorbed oxygen and other unpoisoned lattice oxygen species, most of formic acid were still converted into H_2O and CO_2 . So activity of the catalyst was suppressed, but not seriously deactivated. For $\text{Pt}_{\text{np}}/\text{meso-Fe}_2\text{O}_3$, SO_2 was preferentially adsorbed at the Pt NPs active sites to form sulfate, leading to its poisoning. When the Pt NPs were

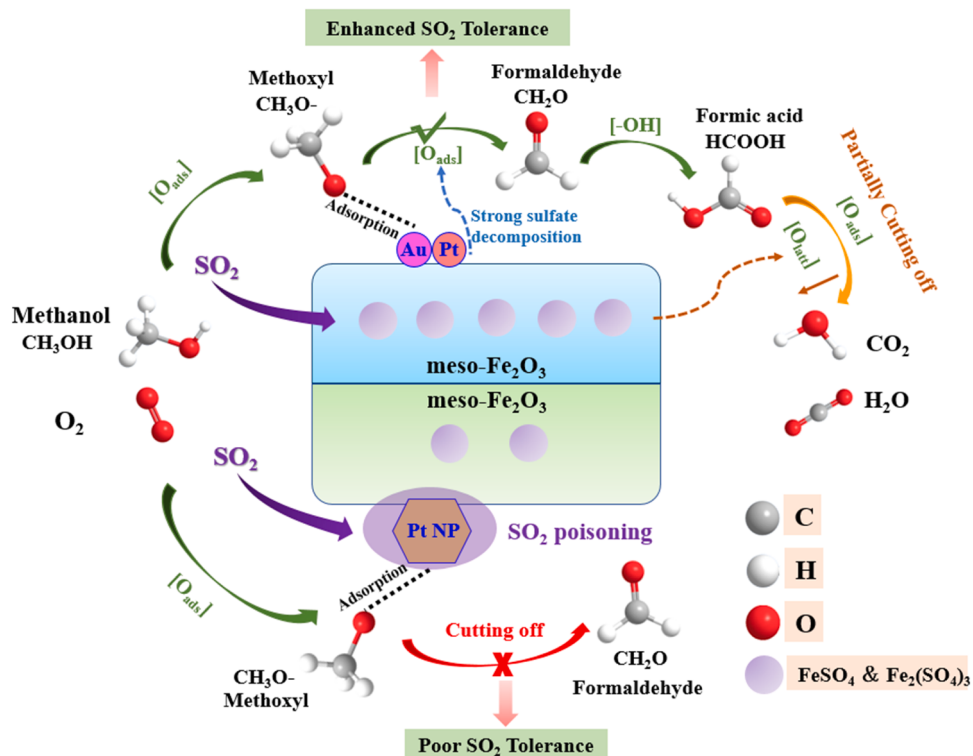


Fig. 8. Proposed mechanism of methanol oxidation over the $\text{Au}_1\text{Pt}_1/\text{meso-Fe}_2\text{O}_3$ and $\text{Pt}_{\text{np}}/\text{meso-Fe}_2\text{O}_3$ catalysts in the presence of SO_2 .

poisoned and difficult to regenerate, however, the cleavage of the C–H bond in the methoxy species adsorbed on its surface was inhibited and the reaction path was suspended, leading to a sharp decline in methanol oxidation activity. Therefore, the active site of Au_1Pt_1 was conducive to the decomposition of sulfates and inhibited the irreversible binding of SO_2 on its surface. On the other hand, meso- Fe_2O_3 acted as a sacrificial site to protect the active sites by storing large amounts of SO_2 , making Au_1Pt_1 /meso- Fe_2O_3 exhibit superior SO_2 tolerance.

4. Conclusions

In summary, the meso- Fe_2O_3 -supported bimetallic Au–Pt single-atom catalyst was successfully prepared. Compared with supported Pt NPs and Pt single-atom catalysts, the Au_1Pt_1 /meso- Fe_2O_3 catalyst exhibited the best activity, giving rise to the 90% methanol conversion at 137 °C and $\text{TOF}_{\text{Noble metal}} = 6.51 \times 10^{-2} \text{ s}^{-1}$ at 120 °C. The high activity is associated with the enhanced reducibility, improved methane adsorption ability and the strong interaction between single-atomic dispersed Au and Pt and meso- Fe_2O_3 . Au_1Pt_1 /meso- Fe_2O_3 also shows the best resistance to SO_2 due to the unique bimetallic atomic active sites that promote its strong sulfate decomposition ability and prevent it from being poisoned. For $\text{Pt}_{\text{np}}/\text{meso-Fe}_2\text{O}_3$, Pt NPs as the active sites were easily poisoned by SO_2 . As a result, the key step (the first C–H bond activation in methoxy species assisted by SMSI) in the reaction process was affected, resulting in severe deactivation. However, SO_2 prone to adsorb on Fe_2O_3 to form iron sulfates over the Au_1Pt_1 /meso- Fe_2O_3 catalyst, preventing the irreversible bonding of SO_2 with the active sites of Au_1Pt_1 . Therefore, combined with the strong sulfates decomposition ability of Au–Pt atomic structure and the sacrificial function of meso- Fe_2O_3 by storing SO_2 , the catalyst exhibits better SO_2 resistance.

CRediT authorship contribution statement

Wenbo Pei: Carried out experiments, wrote and modified the manuscript. **Kuan Yang, Yuxi Liu, Zhiqian Hou, Jia Wang, Yuan Feng, and Xiaohui Yu:** Analyzed the experimental results. **Jiguang Deng and Hongxing Dai:** Designed the experiments, analyzed the experimental results, wrote and modified the manuscript.

Declaration of Competing Interest

We certify that this manuscript entitled “ SO_2 -tolerant mesoporous iron oxide supported bimetallic single atom catalyst for methanol removal” consists of original, unpublished work which is not under consideration for publication elsewhere, and declare no competing financial interest.

Data Availability

Data will be made available on request.

Acknowledgements

This work was supported by the National Natural Science Foundation of China (21876006, 21677004, and 21976009), and National Natural Science Committee of China–Liaoning Provincial People’s Government Joint Fund (U1908204).

Supplementary data

Supplementary material related to this article can be found, in the online version, at doi:<https://doi.org/10.1016/j.apcatb.2023. XXX>.

Appendix A. Supporting information

Supplementary data associated with this article can be found in the

online version at doi:10.1016/j.apcatb.2023.122888.

References

- [1] S. Zhao, K.Z. Li, S. Jiang, J.H. Li, Pd–Co based spinel oxides derived from pd nanoparticles immobilized on layered double hydroxides for toluene combustion, *Appl. Catal. B* 181 (2016) 236–248.
- [2] L. Zhang, Y. Yang, Y.Z. Li, J.C. Wu, S.W. Wu, X. Tan, Q.Q. Hu, Highly efficient UV-visible-infrared photothermocatalytic removal of ethyl acetate over a nanocomposite of CeO_2 and Ce-doped manganese oxide, *Chin. J. Catal.* 43 (2022) 379–390.
- [3] M. Zeng, Y.Z. Li, M.Y. Mao, J.L. Bai, L. Ren, X.J. Zhao, Synergetic effect between photocatalysis on TiO_2 and Thermocatalysis on CeO_2 for gas-phase oxidation of benzene on $\text{TiO}_2/\text{CeO}_2$ nanocomposites, *ACS Catal.* 5 (2015) 3278–3286.
- [4] J.T. Hou, L.L. Liu, Y.Z. Li, M.Y. Mao, H.Q. Lv, X.J. Zhao, Tuning the K^+ concentration in the tunnel of OMS-2 nanorods leads to a significant enhancement of the catalytic activity for benzene oxidation, *Environ. Sci. Technol.* 47 (2013) 13730–13736.
- [5] J.T. Hou, Y.Z. Li, L.L. Liu, L. Ren, X.J. Zhao, Effect of giant oxygen vacancy defects on the catalytic oxidation of OMS-2 nanorods, *J. Mater. Chem. A* 1 (2013) 6736–6741.
- [6] C.T. Yang, G. Miao, Y.H. Pi, Q.B. Xia, J.L. Wu, Z. Li, J. Xiao, Abatement of various types of VOCs by adsorption/catalytic oxidation: A review, *Chem. Eng. J.* 370 (2019) 1128–1153.
- [7] H. Chu, W.T. Lee, K.H. Horng, T.K. Tseng, The catalytic incineration of $(\text{CH}_3)_2\text{S}$ and its mixture with CH_3SH over a $\text{Pt}/\text{Al}_2\text{O}_3$ catalyst, *J. Hazard. Mater.* 82 (2001) 43–53.
- [8] H.L. Chiang, T.C. Chen, J.H. Tsai, Y.C. Hsu, Pollutant characteristics of the pyrolysis of petrochemical wastewater sludge by an electric furnace, *Water Sci. Technol.* 42 (2000) 37–41.
- [9] J.G. Deng, J.B. Zhou, L.P. Gao, Y.L. Zhang, Y.S. Niu, Discussion on treatment technology of overflowing waste gas in silicone desulfurization regeneration tank, *Earth Environ. Sci.* 450 (2020), 012089.
- [10] S. Zhao, K.Z. Li, S. Jiang, J.H. Li, Pd–Co based spinel oxides derived from pd nanoparticles immobilized on layered double hydroxides for toluene combustion, *Appl. Catal. B* 181 (2016) 236–248.
- [11] B. Solsona, T. García, R. Sanchis, M.D. Soriano, M. Moreno, E. Rodríguez-Castellón, S. Agouram, A. Dejoz, J.M. López Nieto, Total oxidation of VOCs on mesoporous iron oxide catalysts: Soft chemistry route versus hard template method, *Chem. Eng. J.* 290 (2016) 273–281.
- [12] B. Darif, S. Ojalaa, L. Pirault-Royc, M. Bensitel, R. Brahmi, R.L. Keiski, Study on the catalytic oxidation of DMDS over Pt–Cu catalysts supported on Al_2O_3 , AlSi_{20} and SiO_2 , *Appl. Catal., B* 181 (2016) 24–33.
- [13] L.A. Calzada, S.E. Collins, C.W. Han, V. Ortalan, R. Zanella, Synergetic effect of bimetallic Au–Ru/ TiO_2 catalysts for complete oxidation of methanol, *Appl. Catal., B* 207 (2017) 79–92.
- [14] M.J. Cheng, E.L. Clark, H.H. Pham, A.T. Bell, M. Head-Gordon, Quantum mechanical screening of single-atom bimetallic alloys for the selective reduction of CO_2 to C_1 hydrocarbons, *ACS Catal.* 6 (2016) 7769–7777.
- [15] J.S. Jirkovsky, I. Panas, E. Ahlberg, M. Halasa, S. Romani, D.J. Schiffrin, Single atom hot-spots at Au–Pd nanoalloys for electrocatalytic H_2O_2 production, *J. Am. Chem. Soc.* 133 (2011) 19432–19441.
- [16] F.R. Lucci, J. Liu, M.D. Marcinkowski, M. Yang, L.F. Allard, M. Flytzani-Stephanopoulos, E.C.H. Sykes, Selective hydrogenation of 1,3-butadiene on platinum–copper alloys at the single-atom limit, *Nat. Commun.* 6 (2015) 8550–8558.
- [17] G. Kyriakou, M.B. Boucher, A.D. Jewell, E.A. Lewis, T.J. Lawton, A.E. Baber, H. L. Tierney, M. Flytzani-Stephanopoulos, E.C.H. Sykes, Isolated metal atom geometries as a strategy for selective heterogeneous hydrogenations, *Science* 335 (2012) 1209–1212.
- [18] M. Guo, P.J. Ma, J.Y. Wang, H.X. Xu, K. Zheng, D.J. Cheng, Y.X. Liu, G.S. Guo, H. X. Dai, E.H. Duan, J.G. Deng, Synergy in Au–CuO Janus structure for catalytic isopropanol oxidative dehydrogenation to acetone, *Angew. Chem. Int. Ed.* 61 (2022), e202203827.
- [19] Z.Q. Hou, L.Y. Dai, J.G. Deng, G.F. Zhao, L. Jing, Y.S. Wang, X.H. Yu, R.Y. Gao, X. R. Tian, H.X. Dai, D.S. Wang, Y.X. Liu, Electronically engineering water resistance in methane combustion with an atomically dispersed tungsten on PdO catalyst, *Angew. Chem. Int. Ed.* 134 (2022), e202201655.
- [20] W.H. Luo, Y. Wang, L.X. Luo, S. Gong, M.N. Wei, Y.X. Li, X.P. Gan, Y.Y. Zhao, Z. H. Zhu, Z. Li, Single-atom and bimetallic nanoalloy supported on nanotubes as a bifunctional electrocatalyst for ultrahigh-current-density overall water splitting, *ACS Catal.* 12 (2022) 1167–1179.
- [21] G.X. Pei, X.Y. Liu, X.F. Yang, L.L. Zhang, A.Q. Wang, L. Li, H. Wang, X.D. Wang, T. Zhang, Performance of Cu-alloyed Pd single-atom catalyst for semihydrogenation of acetylene under simulated front-end conditions, *ACS Catal.* 7 (2017) 1491–1500.
- [22] L.L. Zhang, A.Q. Wang, J.T. Miller, X.Y. Liu, X.F. Yang, W.T. Wang, L. Li, Y. Q. Huang, C.Y. Mou, T. Zhang, Efficient and durable Au alloyed Pd single-atom catalyst for the Ullmann reaction of aryl chlorides in water, *ACS Catal.* 4 (2014) 1546–1553.
- [23] K. Zhao, X. Quan, Y. Su, X. Qin, S. Chen, H.T. Yu, Enhanced chlorinated pollutant degradation by the synergistic effect between dechlorination and hydroxyl radical oxidation on a bimetallic single-atom catalyst, *Environ. Sci. Technol.* 55 (2021) 14194–14203.

[24] Q.Y. Wang, K.L. Yeung, M.A. Bañares, Ceria and its related materials for VOC catalytic combustion: A review, *Catal. Today* 356 (2020) 141–154.

[25] B.S. Kim, J.M. Bae, H.J. Jeong, C.Y. Choe, H. Lee, Surface restructuring of supported nano-ceria for improving sulfur resistance, *ACS Catal.* 11 (2021) 7154–7159.

[26] Q. Yuan, Y.T. Gu, S.Q. Feng, X.G. Song, J.L. Mu, B. Li, X.J. Li, Y.T. Cai, M. Jiang, L. Yan, J.W. Li, Z. Jiang, Y.X. Wei, Y.J. Ding, Sulfur-promoted hydrocarboxylation of olefins on heterogeneous single-Rh-site catalysts, *ACS Catal.* 12 (2022) 4203–4215.

[27] X.H. Yu, Y. Ren, D. Yu, M.Z. Chen, L.Y. Wang, R.D. Wang, X.Q. Fan, Z. Zhao, K. Cheng, Y.S. Chen, J. Gryboś, A. Kotarba, Z. Sojka, Y.C. Wei, J. Liu, Hierarchical porous K-OMS-2/3DOM-m Ti0.7Si0.3O2 catalysts for soot combustion: easy preparation, high catalytic activity, and good resistance to H2O and SO2, *ACS Catal.* 11 (2021) 5554–5571.

[28] F. Liu, K. Asakura, H. He, W. Shan, X. Shi, C. Zhang, Influence of sulfation on iron titanate catalyst for the selective catalytic reduction of NO_x with NH₃, *Appl. Catal.*, B 103 (2011) 369–377.

[29] L. Kang, L.P. Han, P.L. Wang, C. Feng, J.P. Zhang, T.T. Yan, J. Deng, L.Y. Shi, D. S. Zhang, SO₂-tolerant NO_x reduction by marvelously suppressing SO₂ adsorption over Fe_{0.5}Ce_{1-δ}VO₄ catalysts, *Environ. Sci. Technol.* 54 (2020) 14066–14075.

[30] L. Kang, L.P. Han, J.B. He, H.R. Li, T.T. Yan, G.R. Chen, J.P. Zhang, L.Y. Shi, D. S. Zhang, Improved NO_x reduction in the presence of SO₂ by using Fe₂O₃-promoted halloysite-supported CeO₂–WO₃ catalysts, *Environ. Sci. Technol.* 53 (2019) 938–945.

[31] Z.Q. Hou, L.Y. Dai, Y.X. Liu, J.G. Deng, L. Jing, W.B. Pei, R.Y. Gao, Y. Feng, H. X. Dai, Highly efficient and enhanced sulfur resistance supported bimetallic single-atom palladium–cobalt catalysts for benzene oxidation, *Appl. Catal. B* 285 (2021), 119844.

[32] X.F. Zhang, Y.X. Liu, J.G. Deng, L. Jing, L.K. Wu, H.X. Dai, Catalytic performance and SO₂ resistance of zirconia-supported platinum–palladium bimetallic nanoparticles for methane combustion, *Catal. Today* 402 (2022) 138–148.

[33] X.Q. Hao, J.G. Deng, Y.X. Liu, L. Jing, J. Wang, Z.W. Wang, H.X. Dai, Mesoporous Na₂MnO₃-supported platinum–cobalt bimetallic single-atom catalysts with good sulfur dioxide tolerance in propane oxidation, *ACS Sustain. Chem. Eng.* 10 (2022) 8326–8341.

[34] K. Yang, Y.X. Liu, J.G. Deng, X.T. Zhao, J. Yang, Z. Han, Z.Q. Hou, H.X. Dai, Three-dimensionally ordered mesoporous iron oxide-supported single-atom platinum: Highly active catalysts for benzene combustion, *Appl. Catal. B* 244 (2019) 650–659.

[35] W.C. Li, X.Y. Wen, X.J. Wang, J. Li, E.B. Ren, Z.F. Shi, C.M. Liu, D.Q. Mo, S.P. Mo, Oriented growth of δ-MnO₂ nanosheets over core-shell Mn₂O₃@δ-MnO₂ catalysts: An interface-engineered effects for enhanced low-temperature methanol oxidation, *Mol. Catal.* 514 (2021), 111847.

[36] X.Q. Zhang, X.Y. Chen, Y. Liu, M.Y. Guo, Effects of support on performance of methanol oxidation over palladium-only catalysts, *Water Air Soil. Poll.* 231 (2020) 277.

[37] L. Wolski, I. Sobczak, M. Ziolek, Variability of surface components in gold catalysts – The role of hydroxyls and state of gold on activity and selectivity of Au-Nb₂O₅ and Au-ZnNb₂O₆ in methanol oxidation, *J. Catal.* 354 (2017) 100–112.

[38] C. Asokan, L. DeRita, P. Christopher, Using probe molecule FTIR spectroscopy to identify and characterize Pt-group metal based single atom catalysts, *Chin. J. Catal.* 38 (2017) 1473–1480.

[39] M.J. Kale, P. Christopher, Utilizing quantitative *in situ* FTIR spectroscopy to identify well-coordinated Pt atoms as the active site for CO oxidation on Al₂O₃-supported Pt catalysts, *ACS Catal.* 6 (2016) 5599–5609.

[40] X.W. Li, H.X. Dai, J.G. Deng, Y.X. Liu, S.H. Xie, Z.X. Zhao, Y. Wang, G.S. Guo, H. Arandiyani, Au/3DOM LaCoO₃: High-performance catalysts for the oxidation of carbon monoxide and toluene, *Chem. Eng. J.* 228 (2013) 965–975.

[41] H.F. Xiong, S. Lin, J. Goetze, P. Pletcher, H. Guo, L. Kovarik, K. Artyushkova, B. M. Weckhuysen, A.K. Datye, Thermally stable and regenerable platinum–tin clusters for propane dehydrogenation prepared by atom trapping on ceria, *Angew. Chem. Int. Ed.* 56 (2017) 1–7.

[42] G. Fröhlich, W.M.H. Sachtle, Reduction enhancement of Fe₂O₃ in physical mixtures with Pt/mordenite via Pt migration or ‘hydrogen spillover’, *J. Chem. Soc. Faraday Trans.* 94 (1998) 1339–1346.

[43] H.S. Wei, X.Y. Liu, A.Q. Wang, L.L. Zhang, B.T. Qiao, X.F. Yang, Y.Q. Huang, S. Miao, J.Y. Liu, T. Zhang, FeO_x-supported platinum single-atom and pseudosingle-atom catalysts for chemoselective hydrogenation of functionalized nitroarenes, *Nat. Commun.* 5 (2014) 5634–5641.

[44] W.B. Pei, L.Y. Dai, Y.X. Liu, J.G. Deng, L. Jing, K.F. Zhang, Z.Q. Hou, Z. Han, A. Rastegarpanah, H.X. Dai, PtRu nanoparticles partially embedded in the 3DOM Ce_{0.7}Zr_{0.3}O₂ skeleton: Active and stable catalysts for toluene combustion, *J. Catal.* 385 (2020) 274–288.

[45] B. Wang, M.X. Wang, L.N. Han, Y.Q. Hou, W.R. Bao, C.M. Zhang, G. Feng, L. P. Chang, Z.G. Huang, J.C. Wang, Improved activity and SO₂ resistance by Sm-modulated redox of MnCeSmTiO_x mesoporous amorphous oxides for low-temperature NH₃-SCR of NO, *ACS Catal.* 10 (2020) 9034–9045.

[46] C. He, Z.Y. Jiang, M.D. Ma, X.D. Zhang, M. Douthwaite, J.W. Shi, Z.P. Hao, Understanding the promotional effect of Mn₂O₃ on micro-/mesoporous hybrid silica nanocubic-supported Pt catalysts for the low-temperature destruction of methyl ethyl ketone: An experimental and theoretical study, *ACS Catal.* 8 (2018) 4213–4229.

[47] Z.Y. Jiang, X.B. Feng, J.L. Deng, C. He, M. Douthwaite, Y.K. Yu, J. Liu, Z.P. Hao, Z. Zhao, Atomic-scale insights into the low-temperature oxidation of methanol over a single-atom Pt₁-Co₃O₄ catalyst, *Adv. Funct. Mater.* 29 (2019) 1902041.

[48] S. Ordóñez, L. Bello, H. Sastre, R. Rosal, F.V. Diez, Kinetics of the deep oxidation of benzene, toluene, n-hexane and their binary mixtures over a platinum on γ-alumina catalyst, *Appl. Catal., B* 38 (2002) 139–149.

[49] H. Huang, Y. Xu, Q. Feng, D.Y.C. Leung, Low temperature catalytic oxidation of volatile organic compounds: A review, *Catal. Sci. Technol.* 5 (2015) 2649–2669.

[50] C. He, P. Li, J. Cheng, Z.P. Hao, Z.P.A. Xu, comprehensive study of deep catalytic oxidation of benzene, toluene, ethyl acetate, and their mixtures over Pd/ZSM-5 catalyst: Mutual effects and kinetics, *Water Air Soil Pollut.* 209 (2010) 365–376.

[51] Z.Y. Jiang, M.Z. Jing, X.B. Feng, J.C. Xiong, C. He, M. Douthwaite, L.R. Zheng, W. Y. Song, J. Liu, Z.G. Qu, Stabilizing platinum atoms on CeO₂ oxygen vacancies by metal-support interaction induced interface distortion: Mechanism and application, *Appl. Catal. B* 278 (2020), 119304.

[52] S.H. Xie, Y.X. Liu, J.G. Deng, X.T. Zhao, J. Yang, K.F. Zhang, Z. Han, H. Arandiyani, H.X. Dai, Effect of transition metal doping on the catalytic performance of Au-Pd/3DOM Mn₂O₃ for the oxidation of methane and o-xylene, *Appl. Catal. B* 206 (2017) 221–232.

[53] M.N. Khan, L.P. Han, P.L. Wang, J.B. He, B. Yang, T.T. Yan, L.Y. Shi, D.S. Zhang, SO₂-tolerant NO_x reduction over ceria-based catalysts: Shielding effects of hollardite Mn-Ti oxides, *Chem. Eng. J.* 397 (2020), 125535.

[54] E.J. Romano, K.H. Schulz, A. XPS investigation of SO₂ adsorption on ceria-zirconia mixed-metal oxides, *Appl. Surf. Sci.* 246 (2005) 262–270.

[55] Y.Z. Wang, W. Yi, J. Yu, J. Zeng, H.Z. Chang, Novel methods for assessing the SO₂ poisoning effect and thermal regeneration possibility of MO_x–WO₃/TiO₂ (M = Fe, Mn, Cu, and V) catalysts for NH₃-SCR, *Environ. Sci. Technol.* 54 (2020) 12612–12620.

[56] J. Wang, M. Lei, Z.X. Wang, Y.S. Liu, W.C. Zhuang, W.Y. Zhu, Methanol oxidation over rutile Au₁@TiO₂ catalyst: importance of facets and oxygen vacancy, *Appl. Surf. Sci.* 542 (2021), 148541.

[57] K. Routray, L.E. Briand, I.E. Wachs, Is there a relationship between the M=O bond length (strength) of bulk mixed metal oxides and their catalytic activity? *J. Catal.* 256 (2008) 145–153.

[58] J. Xu, S. Guo, F. Hou, J. Li, L.M. Zhao, Methanol oxidation on the PtPd(111) alloy surface: A density functional theory study, *Int. J. Quantum Chem.* 118 (2018), e25491.